ACS APPLIED NANO MATERIALS

www.acsanm.org

Article

Interlayer Excitons and Radiative Lifetimes in $MoSe_2$/SeWS Bilayers: Implications for Light-Emitting Diodes

Renan Narciso Pedrosa, Cesar E. P. Villegas, Alexandre Reily Rocha, Rodrigo G. Amorim,* and Wanderlã Scopel

Cite This: *ACS Appl. Nano Mater.* 2025, 8, 5051−5058

Read Online

ACCESS | Metrics & More | Article Recommendations | Supporting Information

ABSTRACT: Interlayer excitons, formed by electrical charge transfer between layers of 2D van der Waals heterostructures, are of the utmost importance for light-detection and light-harvesting applications. In particular, Janus-based heterostructures are promising platforms to observe robust interlayer exciton dynamics due to their intrinsic electric field. Here, we carry out ground- and excited-state first-principles calculations, based on the G_0W_0 approach and the solution of the Bethe−Salpeter equation, to investigate the energetic, electronic, and excitonic properties of $MoSe_2$/WSSe van der Waals heterobilayers. Our results show that the heterojunction presents features of type-II band alignment and tightly bound, long-lived interlayer excitons. Indeed, the lowest dipole-allowed excitonic state possesses an interlayer character and a slight deviation of 12% in its binding energy compared to the lowest-energy intralayer exciton. Furthermore, the interlayer excitons have transition rates ∼55 times smaller than the intralayer ones, which translates into a longer radiative lifetime of dozens of nanoseconds at room temperature. This is up to 2 orders of magnitude greater than that of the lowest-energy intralayer exciton. The findings emphasize the critical role of Janus-based heterojunctions in influencing interlayer exciton radiative lifetimes, indicating that the system possesses considerable potential for application in optoelectronic devices such as a light-emitting diode (LED) or photodetector.

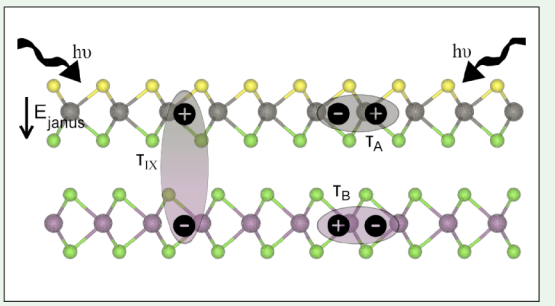

KEYWORDS: *interlayer excitons, $MoSe_2$/SeWS bilayer, radiative lifetimes, G_0W_0, DFT, 2D materials*

INTRODUCTION

The groundbreaking isolation of single-layer graphene[1] paved the way to realize and explore various other two-dimensional (2D) materials,[2−6] revealing promising candidates for different applications in electronics,[7−9] optoeletronics,[10,11] and photovoltaics.[12−16] In particular, group VI transition metal dichalcogenides (TMDCs) have received considerable attention due to their superior stability, tunable electronic and optical properties, as well as their unique excitonic effects.[17,18] Indeed, due to their reduced dimensionality, 2D TMDCs exhibit enhanced excitonic effects that enable to observe other quasi-particle excitations that include biexcitons, trions, and the formation of interlayer excitons,[19−21] some of which possess robust binding energies and can be observed or manipulated even at room temperature.[22,23]

One major progress achieved with 2D materials is the possibility of forming vertically stacked bilayer heterostructures that are bound by weak van der Waals (vdW) interactions. This approach has become the new route to engineer, for instance, various types of band alignments.[24−26] In this regard, type-II band alignment of TMDC-based heterobilayers (HBLs) has been widely studied and demonstrated to be a promising candidate for optical excitation applications.[27−29] In these heterobilayer structures, interlayer excitons, in addition to the intralayer ones, have been observed.[30−33] The former are characterized by presenting small transition rates and longer lifetimes, when compared to the intralayer ones, due to the relatively large electron−hole spatial separation.[32,34] Furthermore, previous studies[35,36] have shown that the interlayer coupling directly impacts the electron−hole pair recombination time. Thus, as the coupling increases, the overlap of the electron−hole wave function enhances, causing the exciton lifetime reduction.[36]

When the vertical spatial symmetry of 2D TMDCs is broken, a new class of layered material, known as Janus TMDC, arises.[37] Experimentally, this can be achieved by replacing the atoms on one of the TMDC's chalcogen layers with another chalcogen element using selective atomic epitaxy replacement.[38] As a result of the symmetry breaking, an out-of-plane intrinsic electric field is formed in the structure.[39] A direct consequence of this effect has been studied in detail for

Received: December 11, 2024
Revised: February 19, 2025
Accepted: February 20, 2025
Published: March 3, 2025

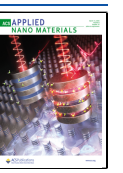

$MoSSe/MoS_2$ and has enabled to observe that the interlayer coupling can be enhanced by up to ∼13% compared to the heterobilayer formed only by MoS_2.[40] Furthermore, it has a considerable impact on the dynamics of interlayer excitons and can aid to extend the exciton radiative lifetime as experimentally demonstrated.[41] This was also shown by Song et al., who found that the carrier lifetime in Janus-based heterobilayers can be tuned depending on the orientation of the Janus monolayers.[42] These findings underscore the importance of Janus-based heterojunctions, especially in the tuning of the interlayer exciton dynamics, which can be pivotal for light-detection and light-harvesting applications.

In this work, we employ *ab initio* density functions and many-body perturbation theories to investigate the structural, energetic, as well as the electronic and excitonic properties of a vertical vdW heterobilayer, formed by $MoSe_2$ and WSSe monolayers. We verified that all interfaces formed are ruled by exothermic processes and have semiconductor character (type-II band alignment), with the bandgap being direct or indirect depending on the stacking pattern. Furthermore, we demonstrate that the most energetically favorable heterostructure presents excitons with binding energies ranging from 0.22 to 0.29 eV. In particular, the structure presents long-lived interlayer excitons with a radiative lifetime of dozens of nanoseconds at room temperature, which is up to 2 orders of magnitude greater than that of the lowest-energy intralayer exciton. The exciton lifetime determined in this study suggests a promising material for light-emitting diodes.

THEORY AND METHODOLOGY

Ground-state density functional theory (DFT) calculations, considering spin−orbit coupling (SOC) and dipole corrections, were carried out to study the energetics and structural properties of $MoSe_2$/WSSe heterostructures by using the Quantum Espresso package.[43] The exchange-correlation energy was obtained within the generalized gradient approximation, as proposed by Perdew, Burke, and Ernzerhof (GGA-PBE),[44] while van der Waals (vdW) interactions were included by considering the Grimme-D2 scheme.[45] Both the pristine monolayers and the $MoSe_2$/WSSe heterobilayer systems consist of one unit cell of 21 Å along the *z*-direction, i.e., between periodic images. Fully relativistic norm-conserving pseudopotentials, obtained from the ONCV database[46] (including 3d semicore states as valence electrons), were used. The Brillouin zone was mapped onto a 9 × 9 × 1 **k**-point mesh, and the Kohn−Sham orbitals were expanded on a plane-wave basis set with an energy cutoff of 85 Ry. Two distinct heterobilayer systems ($MoSe_2$/SWSe and $MoSe_2$/SeWS) were examined, involving six alternative stacking configurations for each one. All structures were fully relaxed to their equilibrium positions with stresses and forces below 0.1 kbar and 2.5 × 10^{-4} eV/Å, respectively.

From the Kohn−Sham eigenstates and eigenvalues, the quasi-particle properties were computed within the G_0W_0 approach considering the plasmon-pole approximation for a **k**-point grid of 24 × 24 × 1. The dielectric screening functions were obtained with an energy cutoff of 60 and 16 Ry for the exchange potential and screened interaction, respectively. We employed the Bruneval−Gonze terminator approach[47] to accelerate the convergence with respect to empty bands, so that 400 bands in the self-energy and 500 bands in the dynamical dielectric screening were enough to reach accurate results (see Figures S1 and S2 for the convergence tests). The Coulomb interaction is described as a truncated potential in slab geometry with an energy cutoff of 6 Ry to reduce spurious interactions among periodic images along the *z*-direction.

The optical spectra were obtained by solving the Bethe−Salpeter equation (BSE), which can be reduced to an eigenvalue problem through the Hamiltonian,

$$H^{exc}_{\substack{vc\mathbf{k}\\ v'c'\mathbf{k}'}} = (\epsilon_{c\mathbf{k}} - \epsilon_{v\mathbf{k}})\delta_{c,c'}\delta_{v,v'}\delta_{\mathbf{k}\mathbf{k}'} + (f_{c\mathbf{k}} - f_{v\mathbf{k}}) \left[2\bar{V}_{\substack{vc\mathbf{k}\\ v'c'\mathbf{k}'}} - W_{\substack{vc\mathbf{k}\\ v'c'\mathbf{k}'}}\right] \quad (1)$$

where the matrix $\left[2\bar{V}_{\substack{vc\mathbf{k}\\ v'c'\mathbf{k}'}} - W_{\substack{vc\mathbf{k}\\ v'c'\mathbf{k}'}}\right]$ is the BSE kernel. Here, the first term corresponds to the electron−hole exchange part from the Hartree potential, while the second term represents the electron−hole attraction from the screened exchange potential. Within the Tamm−Dancoff approximation,[48] the dielectric nature of 2D systems can be described by the imaginary part of the polarizability per unit area,

$$\alpha_2(\omega) = \frac{2\pi e^2}{AN_k}\sum_S \left|\sum_{vc\mathbf{k}} A^S_{vc\mathbf{k}}\hat{\mathbf{e}}\langle c\mathbf{k}|\mathbf{r}|v\mathbf{k}\rangle\right|^2 \delta(\omega - \Omega_S) \quad (2)$$

where $\hat{\mathbf{e}}$ is the polarization vector, and *r* is the position operator. Here, $A^S_{vc\mathbf{k}}$ (Ω_S) is the exciton eigenfunction (eigenvalues) for the *S*-th exciton state, obtained from the diagonalization of the BSE Hamiltonian. Furthermore, N_k is the number of points in the Brillouin zone, and *A* represents the area of the two-dimensional unit cell.

The BSE calculations were carried out by considering a scissor operator applied to the Kohn-Sham energies. The QP correction for the bandgap at the **k**-point was obtained in a 24 × 24 × 1 grid. This simplification can be justified, as we are interested in the lowest energy excitonic states. For all systems, the BSE equation was solved on a finer **k**-grid of 36 × 36 × 1, considering two valence (v) and two conduction (c) bands for the pristine monolayers and four valence and four conduction bands for the heterobilayer structure. In our calculations, we consider light polarized parallel to the plane of the layers and an artificial Lorentzian broadening of 0.05 eV to smear out the optical response. All the quasiparticle calculations were performed using the YAMBO code.[49] All band structures were postprocessed using the YAMBOPY Python library implementation.[50]

The exciton radiative lifetimes at finite temperature are computed using the 2D model proposed by Chen et al.,[51] which has been successfully applied to mono- and bilayer TMDCs[32,35] and also to few-layer black phosphorus.[31] Within this approach, the radiative lifetime of the *S*-th exciton at a finite temperature *T* is defined by the following:

$$\tau_S^{2D}(T) = \gamma_S(T)^{-1} = \gamma_S(0)^{-1} \times \frac{3}{4}\left(\frac{2m_S c^2 k_B T}{\Omega_S(0)^2}\right) \quad (3)$$

where m_S is the effective exciton mass, computed as $m_S = m_e + m_h$, where the first and second right-hand terms are the electron and hole masses, respectively. Ω_S is the *S*-th exciton energy. Here, the recombination rate for the momentum $Q = 0$ is defined as follows:

https://doi.org/10.1021/acsanm.4c06994
ACS Appl. Nano Mater. 2025, 8, 5051−5058

$$\gamma_S(0) = \frac{4\pi e^2 \Omega_S(0) \mu_S^2}{\hbar^2 cA} \quad (4)$$

where A is the area of the unit cell, $\mu_S = \sum_{cvk} A^S_{cvk} d_{cvk}$ are the excitonic transition dipoles, and d_{cvk} are the electronic dipoles computed in the length gauge.

The electron distribution probabilities along the z-axis are computed after the coordinates are integrated perpendicular to the z-direction. The electronic probability in the bottom layer (P(BL)) is obtained by numerically integrating the overlap distribution along the z-axis up to a threshold fixed halfway between the two layers and dividing by the result of integrating the overlap function from 0 to L_z, where L_z represents the lattice parameter along the z-direction. Consequently, the electronic probability in the top layer can be obtained as $P(\mathrm{TL}) = 1 - P(\mathrm{BL})$.

RESULTS AND DISCUSSION

Monolayer Janus WSSe and $MoSe_2$. We start by analyzing the structural and electronic properties of the pristine WSSe and $MoSe_2$ monolayers. Their optimized geometry, depicted in Figure 1a,b, presents a lattice parameter of a = 3.26 Å (3.32 Å) for WSSe ($MoSe_2$). The chalcogen−chalcogen distance is 3.24 Å (3.33 Å) for S−Se (Se−Se), and the bond length is 2.42 Å (2.54 Å) for W−S (W−Se and Mo−Se), respectively. These values are in agreement with the results presented in previous works.[52−55] Figure 1c,d shows the quasi-particle (G_0W_0) electronic structure of WSSe and $MoSe_2$ monolayers, where one observes a direct bandgap energy at **k** symmetry points of 2.59 and 2.38 eV, respectively. The majority contribution to the minimum (maximum) of the conduction (valence) band comes from the constituent transition metal of the monolayer (indicated in red in both cases). In addition, the averaged electrostatic potential for the WSSe monolayer along the z-direction is shown in Figure 1e. There we see a potential difference ΔV = 0.62 eV along the z-direction that determines the orientation of an intrinsic electric field within the monolayer structure. This is a direct consequence of the symmetry breaking along that direction. The relevant electrostatic parameters including the ionization potential (IP), electronic affinity (EA), and work function (Φ) are summarized in Table 1 and agree with previous theoretical studies.[39,55,56]

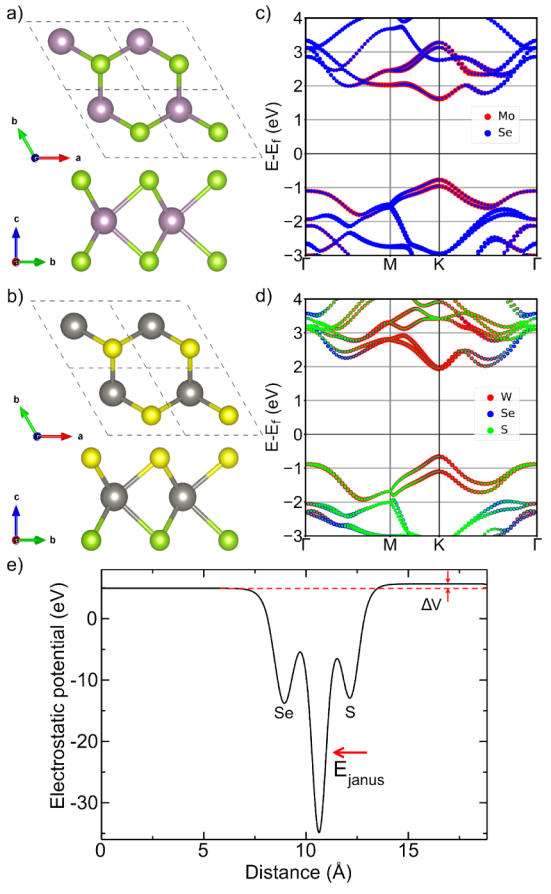

Figure 1. (a, b) The fully relaxed geometry of $MoSe_2$ and the WSSe monolayer. W, Mo, S, and Se atoms are denoted by gray, purple, yellow, and green spheres, respectively. (c, d) The projected quasi-particle electronic band structure of $MoSe_2$ and WSSe monolayer. (e) The electrostatic potential of WSSe.

Table 1. Relevant Electronic and Electrostatic Properties for Pristine WSSe and $MoSe_2$ Monolayers and the HBL AA'-$MoSe_2$/SeWS[a]

Structure	IP (eV)	EA (eV)	Φ (eV)	E_{G0W0} (eV)
WSSe[59]	5.58	4.17	4.93	2.59
$MoSe_2$[55,56]	5.23	3.89	4.46	2.38
AA'-$MoSe_2$/SeWS	4.87	3.93	4.40	1.82

[a]The ionization potential (IP), electronic affinity (EA), and work function (Φ) are obtained at the ground-state level.

Heterobilayers (HBLs). Next, to make the two lattices commensurate for later stacking, we performed an ∼1.8% expansion of WSSe, which implied a reduction in its quasi-particle bandgap of 0.28 eV compared to the pristine one (Figure S3). From this, we constructed two different heterobilayer systems: (i) $MoSe_2$/SWSe and (ii) $MoSe_2$/SeWS. For each of these cases, we considered six different stacking sequences between $MoSe_2$ and WSSe, as depicted in Figure S4, and the band structure is presented in Figure S5. The energetic stability of each one of the heterobilayers was investigated through their formation energy (E_f) (see Table S1).[26] Based on those values, it can be noted that all types of heterobilayers are energetically favorable and an exothermic process drives their formation. In particular, the $MoSe_2$/SeWS heterostructure with AA' stacking (Figure 2a) has E_f= −25.9 meV/Å^2 and is the most energetically stable geometric configuration. These results are comparable with those for other 2D heterobilayer systems.[16,52,57,58] Furthermore, the electrostatic potential (see Figure S6) indicates an intrinsic electric field in the interface, and the dynamical stability of the ($MoSe_2$/SeWS) heterostructure for the AA' configuration was evaluated through phonon dispersion calculations (see Figure S7), and we noticed the absence of negative frequencies, indicating it is stable. We have also studied a stacking configuration in which the Janus sulfur atom points downward (AA'-$MoSe_2$/SWSe). The QP electronic structure and optical absorption for this case are provided in Figure S8a,b.

Focusing on that heterobilayer arrangement, i.e., the AA'-$MoSe_2$/SeWS interface, in Figure 2b, we show the layer-projected electronic structure calculated with quasi-particle corrections. It can be seen that around **k** symmetry point, where the more relevant optical transitions occur, the valence band maximum (VBM) is mostly composed of orbitals from

https://doi.org/10.1021/acsanm.4c06994
ACS Appl. Nano Mater. 2025, 8, 5051−5058

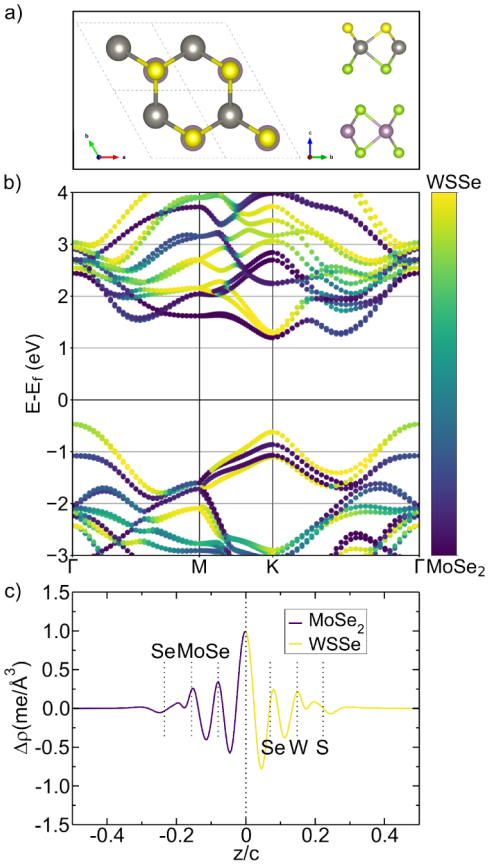

Figure 2. (a) The fully relaxed geometry, (b) the layer-resolved projected electronic band structure, and (c) the plane-averaged charge density difference along the *z*-direction of $MoSe_2$/SeWS-AA' HBL. W, Mo, S, and Se atoms are denoted by gray, purple, yellow, and green spheres, respectively.

the WSSe layer, while the conduction band minimum (CBM) is associated with $MoSe_2$ orbitals. As a consequence, the heterobilayer structure shows a characteristic type-II band alignment, which, in principle, allows for the photogeneration of spatially separated electron−hole pairs with prolonged carrier lifetimes. The isolated constituents (monolayer $MoSe_2$ and WSSe) present a conduction band offset of 0.09 eV, which is slightly lower than that of other similar systems.[30,33] In principle, having a higher conduction band offset implies a higher open-circuit voltage (V_{OC}),[60] which is directly proportional to the efficiency of a photovoltaic device.[60] However, having an adequate value for the conduction band offset (not too large) is essential to have good charge separation without creating unwanted barriers that hinder charge transport, which can negatively impact both the short-circuit current density (J_{SC}) and the filling factor (FF),[61] quantities that limit the efficiency of the device.[60] In addition, we verified that the creation of the interface reduces the quasi-particle bandgap to 1.82 eV in relation to isolated systems, as expected due to quantum confinement effects.

To better understand the charge transfer process in the interface formation and its binding mechanism, Figure 2c shows the planar-averaged charge density difference along the *z*-direction ($\Delta\rho(z)$). Due to the difference in Φ between individual monolayers, when the heterostructure is formed, the Fermi energy level realigns until equilibrium is reached. In response to this realignment, interlayer charge transfer occurs. It is clear that charge densities are redistributed by the formation of regions with gains ($\Delta\rho > 0$) and deficits ($\Delta\rho < 0$) of electrons at the heterostructure interface region. From Bader's analysis,[62] we found that the Janus monolayer loses a charge of $9 \times 10^{-4}e$, while the corresponding charge accumulation is observed in $MoSe_2$, in agreement with type-II band alignment.

Excitonic Effects on Optical Spectra. Figure 3a displays the optical spectra for the $MoSe_2$/SeWS-AA' heterobilayer (green

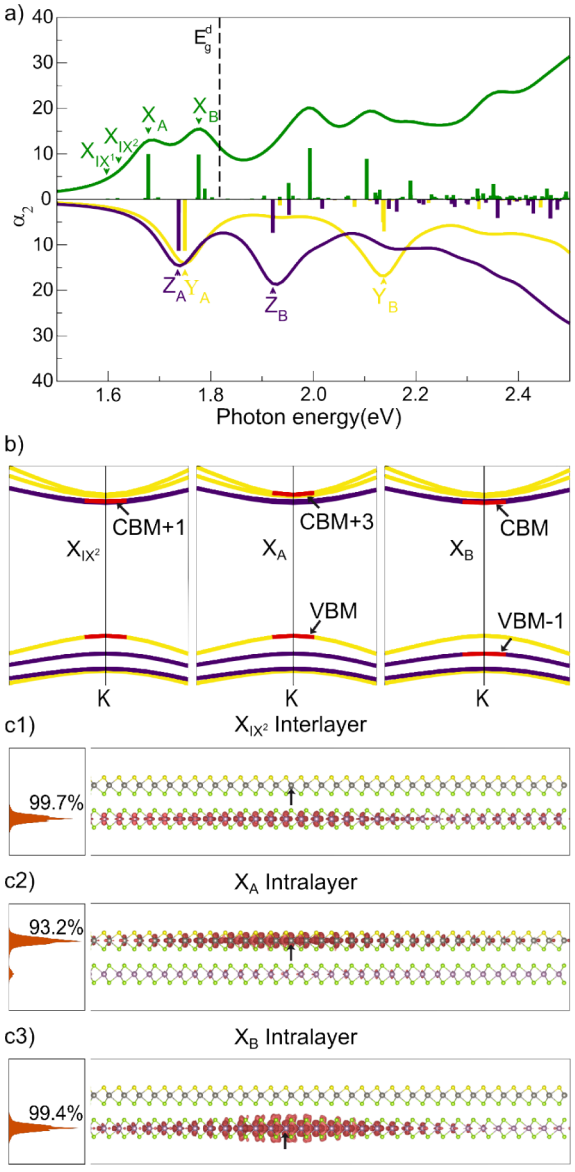

Figure 3. (a) Optical spectra of the $MoSe_2$/SeWS-AA' (green) and the monolayers WSSe (yellow) and $MoSe_2$ (purple), with the respective oscillator strengths (in bars). The vertical black dashed line indicates the value of the direct quasi-particle bandgap of the HBL. (b) QP electronic band structure, around the **k**-point, where the purple (yellow) colors indicate the $MoSe_2$ (WSSe) layer projection. Indicate in red the bands that participate in the respective direct optical transitions. (c) Real space distribution of the electron around the hole position (black arrow), and their corresponding projection along the *z*-axis for (c1) the dipole-allowed interlayer exciton (X_{IX^2}), (c2) the A-exciton (X_A), and (c3) the B-exciton (X_B) state. The integrated electronic probabilities in the hole's layer are shown on the left panel.

https://doi.org/10.1021/acsanm.4c06994
ACS Appl. Nano Mater. 2025, 8, 5051−5058

line) and its corresponding monolayers ($MoSe_2$, purple line and WSSe, yellow line). Hereafter, X_i (with i = IX^1, IX^2, A, and B) denotes the various excitonic states associated with the heterobilayer. The first dipole-allowed transition, X_{IX^1}, is identified as an interlayer exciton with a binding energy of 0.22 eV and possesses a small oscillator strength—only 0.14% of the value of the more intense peak (indicated by the green arrow)—which originates from direct transitions from the valence band maximum (VBM) to the conduction band minimum (CBM) around the **k**-point. Accordingly, X_{IX^2} arises from direct transitions from the VBM to CBM+1 around the **k**-point, with a binding energy of 0.22 eV. Its interlayer character is easily confirmed by the layer-resolved band structure presented in Figure 3b. Since the VBM is predominantly composed of atomic orbitals from the Janus WSSe monolayer and the CBM is associated with the $MoSe_2$ monolayer, this excitation exhibits an interlayer character. This is further confirmed by plotting the electron distribution around the hole position and its corresponding projection along the z-axis, as shown in Figure 3c1. Clearly, 99% of the electron distribution is localized in the $MoSe_2$ layer, while the hole remains in the WSSe layer. These trends are similar to those found in MoS_2/WS_2 heterobilayers, where these states are labeled as "gray" excitons due to their dipole-allowed, although small, oscillator strengths.[63] The small oscillator strength of these interlayer excitons results from the relatively large spatial separation between the electron and the hole. This can be confirmed by assessing their selection rules under symmetry breaking, achieved, for instance, by changing the electric field polarization. Indeed, a comparison of the oscillator strengths of these excitons with those obtained for an out-of-plane polarization of the electric field enables us to confirm that their small oscillator strengths are due to the limited overlap between the electron and hole wave functions (see Figure S9).

The second and third bright excitons, labeled as X_A and X_B, originate from direct transitions from VBM to CBM+3 and VBM−1 to CBM, and they possess binding energies of 0.25 and 0.29 eV, respectively, as indicated in Figure 3b. There, it can be noted that both optical transitions predominantly involve carriers located in the same layer, which determine their intralayer character. A close analysis of the electron probability distribution of X_A and X_B confirms that 93% and 99% of the overall electron distribution are concentrated around the hole layer (see Figure 3c2,c3). Therefore, we confirmed that X_A and X_B are associated with direct transitions within the WSSe and $MoSe_2$ layer, respectively. It is worth mentioning that due to the reduced electron−hole separation in intralayer excitons, the transition rate is almost 55 times greater than that of the interlayer ones. This closely matches the findings for heterostructures based on $MoSe_2$/WSe_2.[30]

For completeness, in Figure 3a, we also present the optical spectra for each individual monolayer, i.e., $MoSe_2$ (purple line) and WSSe (yellow line). It can be verified that, overall, the optical spectrum of HBL is slightly red-shifted in relation to the monolayers. This is expected due to the increase of dielectric screening. However, the intralayer X_A (X_B) exciton presents a red (blue) shift with respect to Y_A (Z_A). This effect could be ascribed to the charge transfer process occurring from the WSSe monolayer to $MoSe_2$.

Table 2 summarizes the relevant values associated with the excitonic spectra of the heterobilayer system, as well as their atomic composition. Interestingly, the system absorbs light in a range of the electromagnetic spectrum desirable for designing

Table 2. Spectral Exciton Position and Exciton Binding Energy Defined as the Difference between the QP Electronic Bandgap and the Optical Gap[a]

$MoSe_2$/SeWS-AA'	X_{IX^1}	X_{IX^2}	X_A	X_B
Composition	W−Mo	W−Mo	W−W	Mo−Mo
Spectral position (eV)	1.60	1.62	1.68	1.78
Binding energy (eV)	0.22	0.22	0.25	0.29

[a]The compositions of the respective exciton are also presented.

tandem solar cells[64] and presents binding energies that may allow exciton transport at room temperature.[65]

Now, we focus on the analysis of the radiative exciton lifetimes, estimated by using eq 3. Table 3 presents the

Table 3. Exciton Radiative Lifetimes for the Monolayer and HBL Systems Indicated in Figure 3a[a]

	$MoSe_2$	WSSe	HBL
τ_A^0 (ps)	0.22	0.20	0.32
τ_B^0 (ps)	0.30	0.29	0.30
$\tau_{IX^2}^0$ (ps)	—	—	18.04
τ_A^{LT} (ps)	20.61	8.25	18.51
τ_B^{LT} (ps)	27.23	12.25	27.38
$\tau_{IX^2}^{LT}$ (ns)	—	—	1.71
τ_A^{RT} (ns)	1.55	0.62	1.39
τ_B^{RT} (ns)	2.04	0.92	2.05
$\tau_{IX^2}^{RT}$ (ns)	—	—	128.32

[a]τ_A (τ_B) refers to the A-excitons (B-excitons) of the monolayers and HBL, while τ_{IX} refers to the interlayer exciton. The calculations were performed at room temperature (RT), 0 K (0), and 4 K (low temperature (LT)).

intrinsic radiative lifetimes at 0 K (τ_i^0), low temperature (τ_i^{LT}), and room temperature (τ_i^{RT}). For the $MoSe_2$ and WSSe monolayers, the intrinsic radiative lifetimes are τ_A^0 [τ_B^0] = 0.22 [0.30] and 0.20 [0.29] ps, respectively. The former result is in excellent agreement with previous studies carried out by Palummo et al.[32] who found values for $\tau_A^0 \sim$ 0.24, 0.22, and 0.19 ps for the $MoSe_2$, WSe_2 and WS_2 monolayers, respectively. For τ_A, we found radiative lifetimes between 8 and 21 ps at low temperature and values smaller than 2 ns at room temperature.

For the interlayer exciton (X_{IX^2}), radiative lifetimes of 18.04 ps, 1.71, and 128.32 ns were obtained for the intrinsic, low temperature, and room temperature regime, respectively. These results indicate that the intrinsic lifetime is ∼2 times (1.5 times) longer than heterobilayers based on $MoSe_2$/WSe_2 (MoS_2/WS_2).[32] For finite temperatures, we found longer radiative lifetimes that are up to 1 order of magnitude longer than that of $MoSe_2$/WSe_2.[32]

More recently, Reho et al.[63] conducted a systematic study on TMDC heterostructures, considering several stacking configurations, including a twisted WSe_2/$MoSe_2$ heterobilayer. They demonstrated that depending on the stacking, the interlayer exciton radiative lifetimes can vary from the picosecond to the nanosecond range. In particular, for the twisted structure, they observed an interlayer exciton with a long-lived lifetime of 428 ns. Furthermore, for light polarized along the plane direction, it was found that dipole-allowed interlayer excitons have lower

https://doi.org/10.1021/acsanm.4c06994
ACS Appl. Nano Mater. 2025, 8, 5051−5058

binding energies when compared to intralayer ones. This is expected since the charge carriers in the interlayer exciton are spatially separated, which reduces their binding energy. However, there is a competition between this separation and the weak Coulomb screening between the layers, which prevents the binding energy of IX excitons from being much lower than that of intralayer excitons.[30]

Regarding the effects of strain, Li et al.[66] showed that in TMDC heterostructures, the binding energy of both interlayer and intralayer excitons decreases with increasing strain. This effect can be exploited as an effective mechanism to tailor the exciton binding energy via in-plane biaxial strain. On the other hand, applying vertical stress to the heterostructure can also impact the excitonic binding energy as verified by Reho et al.[63] Indeed, when varying the interlayer distance in the MoS_2/WS_2 HBL, it was demonstrated that the overlap of the p_z orbitals has a great influence on the optical properties of the system. Although the system under study exhibits strain, based on the aforementioned studies, we expect Janus-based heterobilayer systems with minimal strain to present lower binding energies as well as reduced oscillator strengths.

These sets of results suggest that Janus-based heterobilayers are promising systems for designing optoelectronic devices with longer radiative lifetimes even at room temperature. This can be attributed to the presence of the intrinsic electric field of Janus monolayers that helps to improve the electron−hole spatial separation.[36,42] Moreover, as expected, the radiative lifetimes of the interlayer excitons are significantly longer than those of the intralayers X_A and X_B.

Finally, it is important to highlight that our results indicate that the formation of HBL, when compared to the constituent monolayers, improves the lifetime of the lower energy exciton (IX^2-exciton for HBL and A-exciton for the monolayers). This result, combined with improved manufacturing strategies that suppress nonradiative recombination channels, is essential for improving the efficiency of optoelectronic devices.[67−69] However, when comparing the intralayer excitons of the HBL with those of the monolayers (Y_i and Z_i with i = A, B), it is observed that there were no significant changes in the recombination times, where the HBL times are closer to the lifetimes of the $MoSe_2$ monolayer.

CONCLUSIONS

In summary, we explored the electronic/optical properties of the $MoSe_2$/SeWS heterojunctions using quasi-particle corrections, where the excitonic effects were evaluated through the BSE theory. The electronic results show that the heterojunction presents a semiconducting nature, where the VBM (CBM) is associated with W (Mo) orbitals, indicating that the band alignment is of type-II. Furthermore, we show that the lowest dipole-allowed states (X^1_{IX} and X^2_{IX}) have an interlayer character, presenting binding energies lower than those observed, for example, in MoS_2/WS_2 and $MoSe_2/WSe_2$ heterobilayers. The small oscillator strength of these excitons (dipole-allowed excitons for in-plane polarization, despite their small oscillator strengths of up to 1.6% of the value of the most intense peak) is associated with small overlaps of the electron and hole excitonic wave functions. We have verified this by studying the effect of the out-of-plane electric field polarization, which has the effect of reducing the oscillator strengths by up to 6 orders of magnitude. This suggests that these excitons are sensitive to symmetry breaking, which excludes their dipole-forbidden nature due to spin selection rules. We also found that the interlayer exciton presents an oscillator strength up to 55 times smaller than the intralayer exciton, a value that is slightly higher than conventional TMDC-Se-based HBL. Our lifetimes of the interlayer excitons are up to 2 orders of magnitude higher than those obtained in MoS_2/WS_2 and $MoSe_2/WSe_2$ HBLs, indicating that the system has considerable potential for application as light-emitting diodes.

ASSOCIATED CONTENT

Supporting Information

The Supporting Information is available free of charge at https://pubs.acs.org/doi/10.1021/acsanm.4c06994.

Experimental procedures and characterization data for all new compounds (PDF)

AUTHOR INFORMATION

Corresponding Author

Rodrigo G. Amorim − *Departamento de Física, ICEx, Universidade Federal Fluminense - UFF, Volta Redonda, RJ 27213-145, Brazil;* orcid.org/0000-0001-9611-8772; Email: rgamorim@id.uff.br

Authors

Renan Narciso Pedrosa − *Departamento de Física, Universidade Federal do Espírito Santo- UFES, Vitória, ES 29075-910, Brazil*

Cesar E. P. Villegas − *Departamento de Ciencias, Universidad Privada del Norte, Lima 15434, Peru;* orcid.org/0000-0003-2675-1331

Alexandre Reily Rocha − *Instituto de Física Teórica, Universidade Estadual Paulista (UNESP), São Paulo, SP 01140-070, Brazil;* orcid.org/0000-0001-8874-6947

Wanderlã Scopel − *Departamento de Física, Universidade Federal do Espírito Santo- UFES, Vitória, ES 29075-910, Brazil;* orcid.org/0000-0002-2091-8121

Complete contact information is available at: https://pubs.acs.org/10.1021/acsanm.4c06994

Funding

The Article Processing Charge for the publication of this research was funded by the Coordenacao de Aperfeicoamento de Pessoal de Nivel Superior (CAPES), Brazil (ROR identifier: 00x0ma614).

Notes

The authors declare no competing financial interest.

ACKNOWLEDGMENTS

The authors acknowledge financial support from the Brazilian agencies CAPES (001), CNPq, FAPERJ, INCT Materials Informatics, and FAPES (TO-1043/2022). A.R.R. acknowledges the FAPESP agency (2021/14335-0, 2023/09820-2, and 2023/11751-9). This work used the computational resources of Sci-Com/ES, CEMUCAD/VR, and CENAPAD-SP.

REFERENCES

(1) Novoselov, K. S.; Geim, A. K.; Morozov, S. V.; Jiang, D.; Katsnelson, M. I.; Grigorieva, I. V.; Dubonos, S. V.; Firsov, A. A. Two-dimensional gas of massless Dirac fermions in graphene. *Nature* **2005**, *438*, 197−200.

(2) Pedrosa, R. N.; Amorim, R. G.; Scopel, W. L. Embedded carbon nanowire in black phosphorene and C-doping: the rule to control electronic properties. *Nanotechnology* **2020**, *31*, 275201.
(3) Villegas, C. E.; Rodin, A.; Carvalho, A.; Rocha, A. Two-dimensional exciton properties in monolayer semiconducting phosphorus allotropes. *Phys. Chem. Chem. Phys.* **2016**, *18*, 27829−27836.
(4) Procopio, E. F.; Pedrosa, R. N.; de Souza, F. A. L.; Paz, W. S.; Scopel, W. L. Tuning the photocatalytic water-splitting capability of two-dimensional α-In 2 Se 3 by strain-driven band gap engineering. *Phys. Chem. Chem. Phys.* **2020**, *22* (6), 3520−3526.
(5) Villegas, C. E.; Rocha, A. R. Near-Infrared Optical Response and Carrier Dynamics for High Photoconversion in Tellurene. *J. Phys. Chem. C* **2022**, *126*, 6129−6134.
(6) Zhang, Y.; Wu, J.; Jia, L.; Jin, D.; Jia, B.; Hu, X.; Moss, D.; Gong, Q. Advanced optical polarizers based on 2D materials. *Npj Nanophoton.* **2024**, *1* (1), 28.
(7) Lemme, M. C.; Akinwande, D.; Huyghebaert, C.; Stampfer, C. 2D materials for future heterogeneous electronics. *Nat. Commun.* **2022**, *13* (1), 1392.
(8) Perez, A.; Amorim, R. G.; Villegas, C. E. P.; Rocha, A. R. Nanogap-based all-electronic DNA sequencing devices using MoS 2 monolayers. *Phys. Chem. Chem. Phys.* **2020**, *22*, 27053−27059.
(9) Jadwiszczak, J.; Kelly, D. J.; Guo, J.; Zhou, Y.; Zhang, H. Plasma Treatment of Ultrathin Layered Semiconductors for Electronic Device Applications. *ACS Appl. Electron. Mater.* **2021**, *3*, 1505−1529.
(10) Gupta, A.; Sakthivel, T.; Seal, S. Recent development in 2D materials beyond graphene. *Prog. Mater. Sci.* **2015**, *73*, 44−126.
(11) Tang, Z.; Chen, S.; Li, D.; Wang, X.; Pan, A. Two-dimensional optoelectronic devices for silicon photonic integration. *J. Materiomics* **2023**, *9*, 551−567.
(12) Britnell, L.; Ribeiro, R. M.; Eckmann, A.; Jalil, R.; Belle, B. D.; Mishchenko, A.; Kim, Y.-J.; Gorbachev, R. V.; Georgiou, T.; Morozov, S. V.; Grigorenko, A. N.; Geim, A. K.; Casiraghi, C.; Neto, A. H. C.; Novoselov, K. S. Strong light-matter interactions in heterostructures of atomically thin films. *Science* **2013**, *340*, 1311−1314.
(13) Li, M.-Y.; Chen, C.-H.; Shi, Y.; Li, L.-J. Heterostructures based on two-dimensional layered materials and their potential applications. *Mater. Today* **2016**, *19*, 322−335.
(14) Bernardi, M.; Palummo, M.; Grossman, J. C. Extraordinary sunlight absorption and one nanometer thick photovoltaics using two-dimensional monolayer materials. *Nano Lett.* **2013**, *13*, 3664−3670.
(15) Villegas, C. E. P.; Rocha, A. Elucidating the optical properties of novel heterolayered materials based on MoTe2−InN for photovoltaic applications. *J. Phys. Chem. C* **2015**, *119*, 11886−11895.
(16) Pedrosa, R. N.; Villegas, C. E.; Rocha, A.; Amorim, R. G.; Scopel, W. L. Optical properties enhancement via WSSe/silicene solar cell junctions. *Energy Adv.* **2024**, *3*, 821−828.
(17) Gillespie, S. C.; van der Laan, M.; Poonia, D.; Maiti, S.; Kinge, S.; Siebbeles, L. D.; Schall, P. Optical signatures of charge-and energy transfer in TMDC/TMDC and TMDC/perovskite heterostructures. *2D Mater.* **2024**, *11*, 022005.
(18) Villegas, C. E.; Marinho, E.; Venezuela, P.; Rocha, A. R. Optical spectra and exciton radiative lifetimes in bulk transition metal dichalcogenides. *Phys. Chem. Chem. Phys.* **2024**, *26*, 13251−13260.
(19) Sharma, A.; Zhu, Y.; Halbich, R.; Sun, X.; Zhang, L.; Wang, B.; Lu, Y. Engineering the dynamics and transport of excitons, trions, and biexcitons in monolayer WS2. *ACS Appl. Mater. Interfaces* **2022**, *14*, 41165−41177.
(20) Fang, H.; Lin, Q.; Zhang, Y.; Thompson, J.; Xiao, S.; Sun, Z.; Malic, E.; Dash, S. P.; Wieczorek, W. Localization and interaction of interlayer excitons in MoSe2/WSe2 heterobilayers. *Nat. Commun.* **2023**, *14* (1), 6910.
(21) Wu, B.; Wang, Y.; Zhong, J.; Zeng, C.; Madoune, Y.; Zhu, W.; Liu, Z.; Liu, Y. Observation of double indirect interlayer exciton in MoSe2/WSe2 heterostructure. *Nano Res.* **2022**, *15*, 2661−2666.
(22) Mohamed, N. B.; Lim, H. E.; Wang, F.; Koirala, S.; Mouri, S.; Shinokita, K.; Miyauchi, Y.; Matsuda, K. Long radiative lifetimes of excitons in monolayer transition-metal dichalcogenides MX2 (M= Mo, W; X= S, Se). *Appl. Phys. Express.* **2018**, *11*, 015201.
(23) Robert, C.; Lagarde, D.; Cadiz, F.; Wang, G.; Lassagne, B.; Amand, T.; Balocchi, A.; Renucci, P.; Tongay, S.; Urbaszek, B.; Marie, X. Exciton radiative lifetime in transition metal dichalcogenide monolayers. *Phys. Rev. B* **2016**, *93* (20), 205423.
(24) Li, Q.; Chen, K.-Q.; Tang, L.-M. Large valley splitting in van der Waals heterostructures with type-III band alignment. *Phys. Rev. Appl.* **2020**, *13*, 014064.
(25) Idrees, M.; Amin, B.; Chen, Y.; Yan, X. Design of novel type-I (type-II) band alignment in GeC-VXY (V= Cl, Br; Y= Se, Te) van der Waals heterostructure for optoelectronic and renewable energy application. *Appl. Surf. Sci.* **2023**, *615*, 156260.
(26) Vu, T. V.; Hieu, N. V.; Phuc, H. V.; Hieu, N. N.; Bui, H.; Idrees, M.; Amin, B.; Nguyen, C. V. Graphene/WSeTe van der Waals heterostructure: Controllable electronic properties and Schottky barrier via interlayer coupling and electric field. *Appl. Surf. Sci.* **2020**, *507*, 145036.
(27) Cheng, R.; Li, D.; Zhou, H.; Wang, C.; Yin, A.; Jiang, S.; Liu, Y.; Chen, Y.; Huang, Y.; Duan, X. Electroluminescence and photocurrent generation from atomically sharp WSe2/MoS2 heterojunction p−n diodes. *Nano Lett.* **2014**, *14*, 5590−5597.
(28) Hong, X.; Kim, J.; Shi, S.-F.; Zhang, Y.; Jin, C.; Sun, Y.; Tongay, S.; Wu, J.; Zhang, Y.; Wang, F. Ultrafast charge transfer in atomically thin MoS2/WS2 heterostructures. *Nat. Nanotechnol.* **2014**, *9*, 682−686.
(29) Tsai, M.-L.; Su, S.-H.; Chang, J.-K.; Tsai, D.-S.; Chen, C.-H.; Wu, C.-I.; Li, L.-J.; Chen, L.-J.; He, J.-H. Monolayer MoS2 heterojunction solar cells. *ACS Nano* **2014**, *8*, 8317−8322.
(30) Torun, E.; Miranda, H. P.; Molina-Sánchez, A.; Wirtz, L. Interlayer and intralayer excitons in MoS 2/WS 2 and MoSe 2/WSe 2 heterobilayers. *Phys. Rev. B* **2018**, *97*, 245427.
(31) Chen, Y.; Quek, S. Y. Tunable bright interlayer excitons in few-layer black phosphorus based van der Waals heterostructures. *2D Mater.* **2018**, *5*, 045031.
(32) Palummo, M.; Bernardi, M.; Grossman, J. C. Exciton radiative lifetimes in two-dimensional transition metal dichalcogenides. *Nano Lett.* **2015**, *15*, 2794−2800.
(33) Gillen, R.; Maultzsch, J. Interlayer excitons in MoSe 2/WSe 2 heterostructures from first principles. *Phys. Rev. B* **2018**, *97*, 165306.
(34) Rivera; Rivera, P.; Schaibley, J. R.; Jones, A. M.; Ross, J. S.; Wu, S.; Aivazian, G.; Klement, P.; Seyler, K.; Clark, G.; Ghimire, N. J.; Yan, J. Observation of long-lived interlayer excitons in monolayer MoSe2−WSe2 heterostructures. *Nat. Commun.* **2015**, *6* (1), 6242.
(35) Gao, S.; Yang, L.; Spataru, C. D. Interlayer coupling and gate-tunable excitons in transition metal dichalcogenide heterostructures. *Nano Lett.* **2017**, *17*, 7809−7813.
(36) Long, C.; Dai, Y.; Gong, Z.-R.; Jin, H. Robust type-II band alignment in Janus-MoSSe bilayer with extremely long carrier lifetime induced by the intrinsic electric field. *Phys. Rev. B* **2019**, *99*, 115316.
(37) Chaurasiya, R.; Tyagi, S.; Kale, A. J.; Gupta, G. K.; Kumar, R.; Dixit, A. Advances in Physics and Chemistry of Transition Metal Dichalcogenide Janus Monolayers: Properties, Applications, and Future Prospects, *Adv. Theory Sim.*, **2024**, 2400854. .
(38) Li, R.; Cheng, Y.; Huang, W. Recent progress of Janus 2D transition metal chalcogenides: from theory to experiments. *Small* **2018**, *14* (45), 1802091.
(39) Ju, L.; Bie, M.; Tang, X.; Shang, J.; Kou, L. Janus WSSe monolayer: an excellent photocatalyst for overall water splitting. *ACS Appl. Mater. Interfaces* **2020**, *12* (26), 29335−29343.
(40) Zhang, K.; Guo, Y.; Ji, G.; Lu, A.-Y.; Su, C.; Wang, H.; Puretzky, A. A.; Geohegan, D. B.; Qian, X.; Fang, S.; Kaxiras, E.; Kong, J.; Huang, L. Enhancement of van der Waals interlayer coupling through polar Janus MoSSe. *J. Am. Chem. Soc.* **2020**, *142*, 17499−17507.
(41) Zheng; Zheng, T.; Lin, Y.-C.; Yu, Y.; Valencia-Acuna, P.; Puretzky, A. A.; Torsi, R.; Liu, C.; Ivanov, I. N.; Duscher, G.; Geohegan, D. B.; Ni, Z. Excitonic dynamics in janus MoSSe and WSSe monolayers. *Nano Lett.* **2021**, *21* (2), 931−937.

https://doi.org/10.1021/acsanm.4c06994
ACS Appl. Nano Mater. 2025, 8, 5051−5058

(42) Song, B.; Liu, L.; Yam, C. Suppressed carrier recombination in Janus MoSSe bilayer stacks: a time-domain ab initio study. *J. Phys. Chem. Lett.* **2019**, *10*, 5564−5570.
(43) Giannozzi; Giannozzi, P.; Baroni, S.; Bonini, N.; Calandra, M.; Car, R.; Cavazzoni, C.; Ceresoli, D.; Chiarotti, G. L.; Cococcioni, M.; Dabo, I.; Dal Corso, A. QUANTUM ESPRESSO: a modular and open-source software project for quantum simulations of materials. *J. Phys.: condens. Matter* **2009**, *21* (39), 395502.
(44) Perdew, J. P.; Burke, K.; Ernzerhof, M. Generalized gradient approximation made simple. *Phys. Rev. Lett.* **1996**, *77*, 3865.
(45) Grimme, S. Semiempirical GGA-type density functional constructed with a long-range dispersion correction. *J. Comput. Chem.* **2006**, *27*, 1787−1799.
(46) Hamann, D. R. Optimized norm-conserving Vanderbilt pseudopotentials. *Phys. Rev. B* **2013**, *88* (8), 085117.
(47) Bruneval, F.; Gonze, X. Accurate GW self-energies in a plane-wave basis using only a few empty states: Towards large systems. *Phys. Rev. B* **2008**, *78* (8), 085125.
(48) Fetter, A. L.; Walecka, J. D. *Quantum theory of many-particle systems*; Courier Corporation, 2012.
(49) Marini, A.; Hogan, C.; Grüning, M.; Varsano, D. Yambo: an ab initio tool for excited state calculations. *Comput. Phys. Commun.* **2009**, *180*, 1392−1403.
(50) https://github.com/rreho/yambopy.
(51) Chen, H.-Y.; Jhalani, V. A.; Palummo, M.; Bernardi, M. Ab initio calculations of exciton radiative lifetimes in bulk crystals, nanostructures, and molecules. *Phys. Rev. B* **2019**, *100*, 075135.
(52) Zhou, W.; Chen, J.; Yang, Z.; Liu, J.; Ouyang, F. Geometry and electronic structure of monolayer, bilayer, and multilayer Janus WSSe. *Phys. Rev. B* **2019**, *99*, 075160.
(53) Zhang, Y.; Ye, H.; Yu, Z.; Liu, Y.; Li, Y. First-principles study of square phase MX2 and Janus MXY (M= Mo, W; X, Y= S, Se, Te) transition metal dichalcogenide monolayers under biaxial strain. *Phys. E* **2019**, *110*, 134−139.
(54) Ataca, C.; Sahin, H.; Ciraci, S. Stable, single-layer MX2 transition-metal oxides and dichalcogenides in a honeycomb-like structure. *J. Phys. Chem. C* **2012**, *116*, 8983−8999.
(55) Ramasubramaniam, A. Large excitonic effects in monolayers of molybdenum and tungsten dichalcogenides. *Phys. Rev. B* **2012**, *86*, 115409.
(56) Kim, H.-G.; Choi, H. J. Thickness dependence of work function, ionization energy, and electron affinity of Mo and W dichalcogenides from DFT and GW calculations. *Phys. Rev. B* **2021**, *103*, 085404.
(57) Zhang, Y.-F.; Pan, J.; Du, S. Geometric, electronic, and optical properties of MoS2/WSSe van der Waals heterojunctions: a first-principles study. *Nanotechnology* **2021**, *32*, 355705.
(58) Zhang, W.; Yin, Y.; He, C. Lowering the Schottky barrier height of G/WSSe van der Waals heterostructures by changing the interlayer coupling and applying external biaxial strain. *Phys. Chem. Chem. Phys.* **2020**, *22*, 26231−26240.
(59) Thanh; Thanh, V. V.; Van, N. D.; Truong, D. V.; Saito, R.; Hung, N. T. First-principles study of mechanical, electronic and optical properties of Janus structure in transition metal dichalcogenides. *Appl. Surf. Sci.* **2020**, *526*, 146730.
(60) Chen, Y.; Tan, X.; Peng, S.; Xin, C.; Delahoy, A. E.; Chin, K. K.; Zhang, C. The influence of conduction band offset on CdTe solar cells. *J. Electron. Mater.* **2018**, *47*, 1201−1207.
(61) Minemoto, T.; Murata, M. Theoretical analysis on effect of band offsets in perovskite solar cells. *Sol. Energy Mater. Sol. Cells* **2015**, *133*, 8−14.
(62) Henkelman, G.; Arnaldsson, A.; Jónsson, H. A fast and robust algorithm for Bader decomposition of charge density. *Comput. Mater. Sci.* **2006**, *36*, 354−360.
(63) Reho, R.; Botello-Méndez, A.; Sangalli, D.; Verstraete, M.; Zanolli, Z. Excitonic response in transition metal dichalcogenide heterostructures from first principles: Impact of stacking, twisting, and interlayer distance. *Phys. Rev. B* **2024**, *110*, 035118.
(64) Wali, Q.; Elumalai, N. K.; Iqbal, Y.; Uddin, A.; Jose, R. Tandem perovskite solar cells. *Renewable Sustainable Energy Rev.* **2018**, *84*, 89−110.
(65) Unuchek, D.; Ciarrocchi, A.; Avsar, A.; Watanabe, K.; Taniguchi, T.; Kis, A. Room-temperature electrical control of exciton flux in a van der Waals heterostructure. *Nature* **2018**, *560*, 340−344.
(66) Li, L. L.; Gillen, R.; Palummo, M.; Milos0cević, M.; Peeters, F. Strain tunable interlayer and intralayer excitons in vertically stacked MoSe2/WSe2 heterobilayers. *Appl. Phys. Lett.* **2023**, *123* (3), 033102.
(67) Wang, K.; Huo, J.; Cao, L.; Yang, P.; Muüller-Buschbaum, P.; Tong, Y.; Wang, H. Fully Methylammonium-Free Stable Formamidinium Lead Iodide Perovskite Solar Cells Processed under Humid Air Conditions. *ACS Appl. Mater. Interfaces* **2023**, *15*, 13353−13362.
(68) Liu, Q.; Vandewal, K. Understanding and Suppressing Non-Radiative Recombination Losses in Non-Fullerene Organic Solar Cells. *Adv. Mater.* **2023**, *35* (35), 2302452.
(69) Lien, D.-H.; Uddin, S. Z.; Yeh, M.; Amani, M.; Kim, H.; Ager Iii, J. W.; Yablonovitch, E.; Javey, A. Electrical suppression of all nonradiative recombination pathways in monolayer semiconductors. *Science* **2019**, *364*, 468−471.

https://doi.org/10.1021/acsanm.4c06994
ACS Appl. Nano Mater. 2025, 8, 5051−5058